Pre-study of the Dissolution Behavior of Silicon Kerf Residue in Steel

Adamantia Lazou, David Nilssen, Mertol Gökelma, Maria Wallin, and Gabriella Tranell

Abstract Silicon kerf residue is generated during the wafering process of pure silicon in the photovoltaic value chain. The generated by-product has a high volume, and the particle size is typically below 1 μm. Although the fine particles are partly oxidized, the material may be beneficial in different metallurgical applications such as grain refining and alloy composition adjustments. This work studies the dissolution behavior of silicon kerf in low alloy steel melts with the aim to upcycle the kerf material in the steel industry for different purposes. In this study, a steel alloy and the kerf residue were melted (at 1580 °C) in an alumina crucible placed in an induction furnace. The amount of added kerf residue was varied. The behavior of the particles in the solidified alloy was characterized by using an optical microscope, electron probe microscope (EPMA), and wavelength-dispersive X-ray spectroscopy (WDS) in order to study the dissolution behavior of the Si-kerf residue in the steel.

Keywords Silicon kerf residue · Utilization of by-products · Low alloy steels · Melting and dissolution of silicon kerf

Introduction

Solar energy is a clean renewable resource, allowing a rapid increase in worldwide crystalline Si (cSi)-based photovoltaic (PV) distribution over the past couple decades [1]. In the photovoltaic value chain, illustrated in Fig. 1, metallurgical grade silicon (MG-Si) is produced from quartz and carbon reductants. The MG-Si is further purified to solar grade silicon (SoG-Si) through chemical or metallurgical methods. For photovoltaic applications, a typical purity of the SoG-Si is >6 N [2]. Single-

A. Lazou (✉) · D. Nilssen · M. Wallin · G. Tranell
Department of Materials Science and Engineering, Norwegian University of Science and Technology, NTNU, 7034 Trondheim, Norway
e-mail: adamantia.lazou@ntnu.no

M. Gökelma
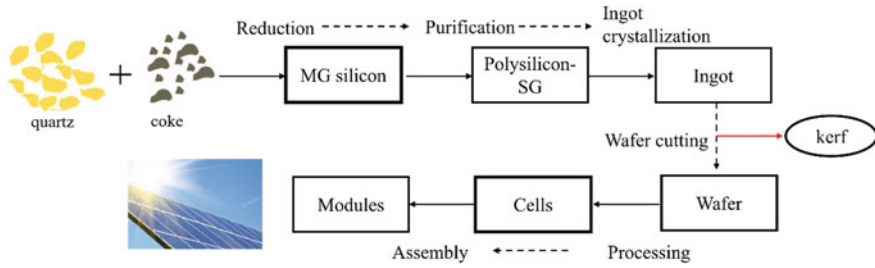Department of Materials Science and Engineering, İzmir Institute of Technology, 35430 İzmir, Turkey

Fig. 1 PV value chain

or multi-crystalline ingots are then produced through crystal pulling or directional solidification. The ingots are cut into blocks which are sliced into wafers, mainly by diamond wire sawing [3, 4]. During this process, approximately 35–40% of crystalline silicon, known as silicon kerf residue, is lost. The material is complex and is usually composed of fine (typically in the order of 1 μm, due to the brittle structure of silicon) partly oxidized silicon particles with some metallic contamination from the sawing wire and lubricants [1, 2, 5]. The disposal of this material represents both a resource loss and creates environmental challenges. The global installed capacity of PV is estimated to reach 1270.5 GW by the end of 2022, mainly through cSi technologies, which is more than 200 times the capacity that was estimated by the end of 2017 [6]. The annual production of Si-kerf is estimated around 168.000 tonnes/year [5]. By effectively valorising Si-kerf residue, the specific process emissions and energy consumption will be reduced in the primary Si production, and less waste will be landfilled.

Research for the recycling of Si-kerf refers among others to use in silicon-containing alloys [7], refining by centrifugation [8], and directional solidification techniques. The recycling of silicon from the Si-kerf is, however, challenging due to the small particle size and impurity content [1, 9]. Hence, the reuse of Si-kerf into other applications reduces the mentioned challenges [1], and the most studied uses are the production of silicon carbide powder, silicon nitride [10], in ceramics, etc. [1].

Perspectives of the Present Study

The use of inoculant agents for grain refining in metal casting is well known. The use of such agents, in the wire and arc additive manufacturing (WAAM), is, however, still under investigation [11]. Recently, the WAAM technology has drawn attention due to the benefits that it can offer to create, repair, and extend the life time of large industrial equipment and in this way reduce the cost and material waste as well as increase the materials efficiency [12]. Nevertheless, challenges exist that are related to the manufacturing accuracy, quality assurance, and automation of the WAAM system

[13]. The formation of large grain size microstructures during the production reduces the mechanical properties of the product which might be detrimental for the material's performance. Considering this, the introduction of inoculating agents during the WAAM process can promote the grain refinement and modify the existing phases. Typical inoculation agents for low alloyed steels are the rare earth metal oxides, NbC-containing ferroalloy, or TiN-containing ferro alloy [14, 15]. One potential inoculant agent for low alloyed steel is SiC particles due to their properties such as high hardness and high melting point [11], opening possibilities for use of carburized kerf residue. The Si-kerf residue could also be used to fine-tune the composition of a steel alloy. Microalloying or modifying the composition of an alloy is a tool to reduce the cost related to post-processing and enhance the properties of alloys [16].

The present study is a preliminary experimental investigation of the dissolution behavior of the Si-kerf residue introduced into a steel melt, which offers the basis for further research and experimental investigations into the potential for recycling and reuse of the kerf in the steel industry. In the current work, the main objectives are being to observe and evaluate the physical interaction and dissolution behavior of the Si particles in steel.

Materials and Methods

The steel used was a commercial low alloy steel (ASTM A182 black rolled bar, EN10204) with chemical composition as listed in Table 1. The steel was received as a rod (Ø76.2 × 2000 mm) which was cut into small pieces prior to the experimental trials. The Si-kerf was received as dried powder material (thermally treated to remove the lubricant), and its chemical composition is presented in Table 1. The steel and Si-kerf samples were dried at 100 °C for 24 h prior to analysis and experimental trial. Approximately 98 g steel was used in each experiment, while the amount of Si-kerf was varied. The Si-kerf particles were introduced and melted together with the steel (before melting) for the experiments presented in the current work (two in total). The amount of kerf was varied between the trials, while the temperature and time were kept constant. The additions of Si-kerf were aimed to achieve, 25 (sample I), and 50 (sample II) times more (wt%) Si in the final alloy that corresponds to approximately 5 and 10 wt%, respectively. A steel sample was melted without the addition of Si-kerf residue particles, to provide the reference comparison for the samples I and II.

Table 1 Chemical composition of steel in weight % and Si-kerf in ppm

Steel	Fe	Cr	Mo	Ni	Si	C	Mn	P	Cu	–	
	Balance	2.34	1.03	0.20	0.21	0.13	0.53	0.01	0.17	–	
Si-kerf	Al	Co	Cr	Cu	Fe	Mg	Ni	Pb	Ti	Zn	Si
	81.4	0.218	2.05	4.45	352	6.74	560	1.49	25.4	7.86	94×10^4

The experiments were conducted in a closed 30 kW induction furnace, in which 5–6 kW corresponds to the temperature range of 1400–1600 °C in the present study (Fig. 2a). The furnace can operate either under vacuum or in controlled atmosphere (Ar in the present study with purity of 99.9% and approximately 1 l/min flow rate). Prior to the experiments, the oxygen was removed from the furnace chamber (0.5–0.6 m³) atmosphere through one-time evacuation and argon flashing up to 1030 mbar. During the experiments, Ar was flowing to the chamber keeping the pressure around 1030–1050 mbar. The experiments were conducted in alumina crucibles (A5, Ø50/44 × 75 mm) that were placed inside a graphite crucible (IG-15, Ø60/52 × 100 mm) (Fig. 2b). The temperature was recorded with the use of a thermocouple type C that was placed in the sample. The heating was controlled with a manual increase of the supplied power, and the target experimental temperature was 1580 °C (±20), to ensure complete melting of the steel (Fig. 2c). After reaching the target temperature, the samples were immediately left to cool to room temperature. The samples were then prepared for electron probe microscope analysis (EPMA) to examine the microstructure, the chemical composition of the product phases, and the distribution of the elements between phases. The EPMA analysis was carried out in a fixed working distance of 11 mm, different magnifications, and an acceleration voltage of 15 kV was applied. The microstructure of the reference sample was analyzed by using scanning electron microscope (SEM). Images were taken in different magnifications, and the composition was measured with energy dispersive spectroscopy (EDS) analysis. The SEM analysis was executed with an acceleration voltage of 15 kV in 10 mm working distance.
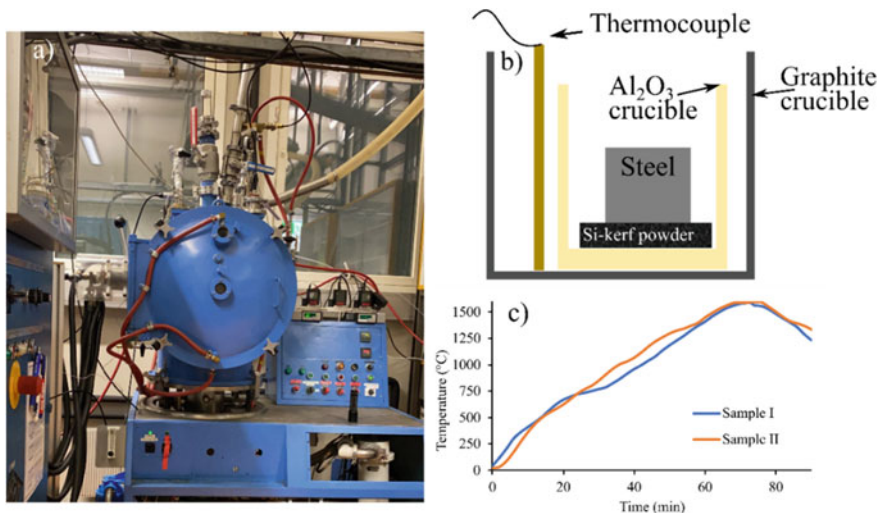

Fig. 2 a Induction furnace used in this work, **b** sample set up (before melting) in the crucible, and **c** temperature profile for the samples I and II

Results and Discussion

The chemical composition of the steel can be seen in Table 1. The steel is a Cr-rich low alloy steel which is commonly used in forged components due to its properties [17, 18]. The initial Si content of the steel was approximately 0.21 wt%. In Table 1, the chemical analysis of the Si-kerf is also presented (in ppm), as measured with ICP-MS analysis. The Si-kerf is mainly composed of Si, while the rest of the elements that were detected are attributed to the sawing process [4]. The balance is attributed mainly to atmospheric impurities such as oxygen and carbon [4].

The SEM analysis of the reference sample (steel melted without additions of Si-kerf residue) can be seen in Fig. 3, and the quantification of the marked points is provided in Table 2. Figure 3a and b presents an overview of the sample in low magnification in secondary and backscatter electron images, respectively. Figure 3c provides an image in higher magnification. The sample is mainly composed of a
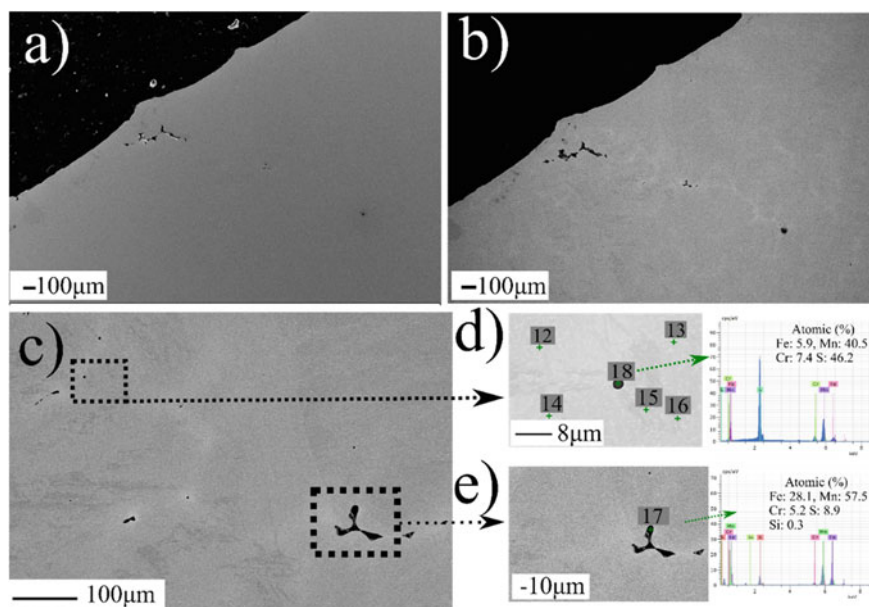

Fig. 3 Micrographs of reference sample **a** secondary, **b, c, d** and **e** backscattered electron images in 100×, 100×, 500×, 5000×, and 1000× magnification, respectively. The magnified areas are marked in the figure. The marked points are quantified in the figure and in Table 2

Table 2 Composition (atomic %) of the reference sample as measured with EDS

Points	Fe	Cr	S	Si	Mn
12–14	94.3	3.1	1.4	0.7	0.8
15–16	95.3	2.7	0.9	0.6	0.7

Fig. 4 Sample II after melting at 1580 °C with immediate cooling (kerf and steel were melted together)
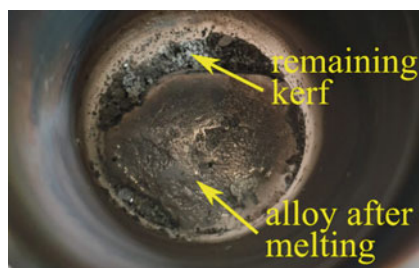
light grey phase (points 12–14), while a slight darker phase (points 15–16) presents in less extend. The difference in their appearance could be attributed to the slight difference in their composition (lower Cr and S for points 15–16).

Figure 3d, e present the analysis of the dark phase which contains a higher Mn, Cr, and S content in comparison with the rest of the analysed points (Table 2).

As mentioned, the samples after melting were prepared for EPMA analysis. Remaining powder was observed after the melting process, attributed to undissolved Si-kerf residue (Fig. 4). This might indicate that the given time at the target temperature was not enough to achieve complete melting of the Si-kerf residue, considering also the added amount of Si-kerf.

The micrographs for sample I can be seen in Fig. 5, and the chemical composition of the different phases is provided in Table 3. Figure 5a, b presents the cross-section of the sample from the upper and inner part, as shown with the arrow. According to Fig. 5a, it seems that in the upper part of the sample there is a dark grey phase that was mainly composed of Si, indicating the presence of remaining Si-kerf. In general, the sample seems to be composed mainly of a bright grey phase A, while a slight darker grey phase B was observed in a random distribution (Fig. 5b). Based on the analysis of the marked phases (Table 3), the major component is Fe, while it seems

Fig. 5 Micrographs of sample I from **a** upper and **b** inner part, in 100× and 1000× magnification, respectively. The magnified area is marked in the figure. Marked phases are quantified in Table 3
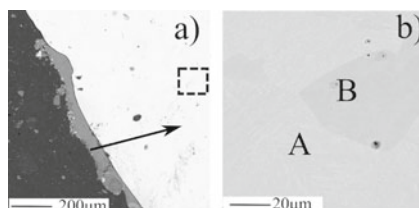

Table 3 Chemical analysis (wt%) of the phases for the sample I, as measured with EPMA

Points	Fe	Cr	Mo	Si	Mn	S
A[a]	95.07	2.39	0.09	2.25	0.53	0.02
B[a]	95.75	2.29	0.13	2.60	0.47	0.03

[a] Average from 5 points

that there is a slight difference in the Si content. Phase B seems to have slightly lower Si concentration.

A mapping analysis might indicate more clear the distribution of elements between these phases. The Si content of these phases is approximately 2% that is lower than the expected (around 5%), confirming that less Si than added was dissolved. Nevertheless, the Si content of the final alloy has increased (around 11% more Si) as compared to the initial alloy. The composition is close to the bcc phase, which indicates that silicon is dissolved in iron rather than forming intermetallic phases. Si seems to be homogenously dissolved in the sample, although it should be emphasized that the size of the Si-kerf particles is small which makes the detection of the particles challenging.

The mapping analysis of the sample I can be seen in Fig. 6. The analysis confirms the observations mentioned earlier as the distribution of Si and Fe seems even between phases A and B. This might indicate further that the difference in the appearance of phase A and B could be attributed on the density difference, possibly due to the higher content of Mo in the B phase. The micrograph of phase A suggest a similar morphology with the reference sample morphology of phase A, although the chemistry of the different phases is changing due to the dissolution of Si-kerf.

The micrographs for sample II can be seen in Fig. 7. The analysis of the marked phases is provided in Table 4. Figure 7a and b presents the cross-section of the
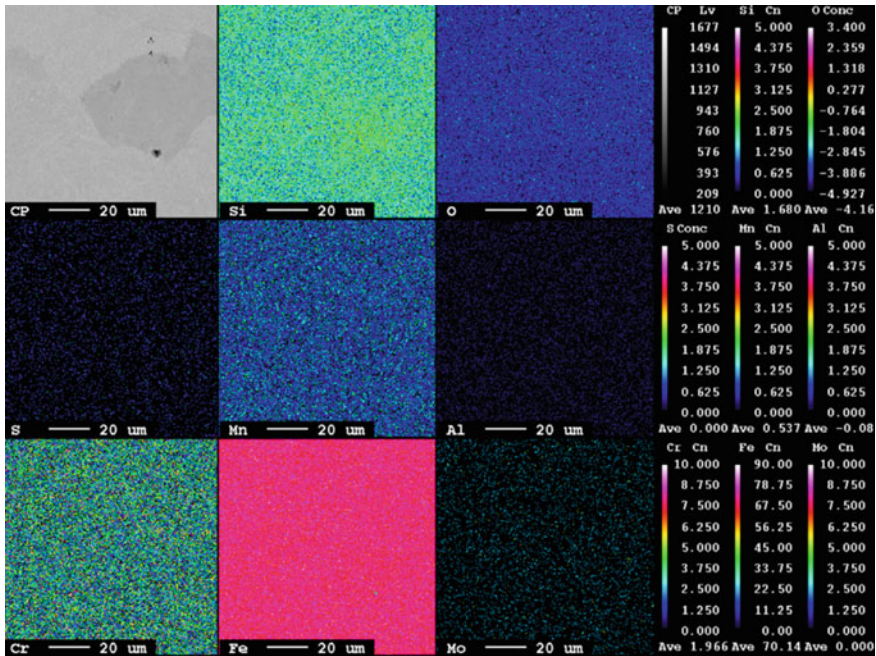

Fig. 6 EPMA map of silicon, oxygen, sulfur, manganese, aluminium, chromium, iron, and molybdenum, for sample I in 1000× magnification
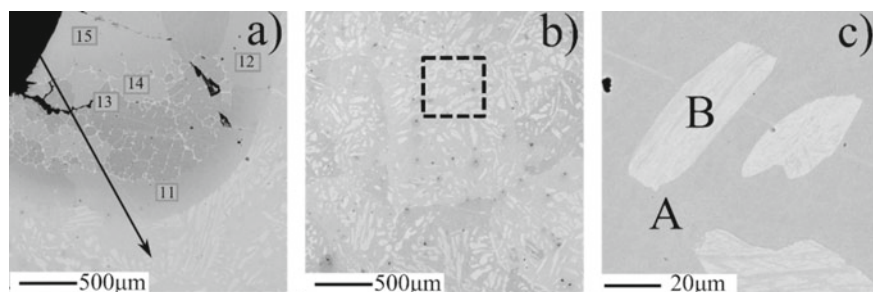
Fig. 7 Micrographs for sample II **a** on the upper part, **b** and **c** in the inner of the sample in 40×, 40×, and 1000× magnification, respectively. The magnified area is marked in the figure. Marked phases are quantified in Table 4

Table 4 Chemical analysis (wt%) of the phases for the sample II, as measured with EPMA

Points	Fe	Cr	Mo	Si	Mn	S
A[a]	94.34	2.35	0.06	3.64	0.53	0.03
B[a]	94.77	2.36	0.04	3.25	0.57	0.01
11–12	90.5	2.08	0.06	8.06	0.48	0.01
13	88.22	1.85	0.01	10.37	0.47	0.04
14	88.06	1.79	–	9.36	0.57	0.01
15	90.3	1.81	0.06	6.48	0.43	0

[a] Average from 5 points

sample from the outer (upper part, not in contact with crucible) and inner parts of the sample, respectively, as shown by the arrow. Figure 7c presents the micrograph from the inner part of the sample in higher magnification than Fig. 7b. Based on Fig. 7a, it seems that in the upper part of the sample, there is a region where the microstructure appears to more homogeneous (dark grey phase) than the inner part. Moreover, this region seems to have clear boundaries with the inner part of the sample.

In this region (points 11–15 in Table 4), there is significantly higher Si content. This might correlate with the fact that in this sample there was remaining kerf, indicating that part of the added Si-kerf remained undissolved. On the other hand, on the inner part of the sample, there are mainly two phases with clear boundaries, the dark grey phase A and brighter grey phase B.

The analysis of these two phases (in Table 4) indicates that their chemical characteristics are similar although the Si content in phase B is slightly lower. Individual SiO_2 particles could, however, not be observed. Moreover, the Si content was higher than in sample I, indicating that more kerf was dissolved in this case. The measured compositions can be seen in Table 4. For the rest of the analyzed points, Si is significantly increased. The morphology and composition of sample II are different than

both the reference sample and sample I. This indicates that the addition of more Si-kerf residue changes the microstructural appearance. However, the effects of dissolution of the Si-kerf residue on the microstructure of the steel need to be addressed in future work.

The particles of Si-kerf residue are believed to contain some amount of SiO_2 on their surface due to oxidation, considering the stability of SiO_2 over Si. As an example, approximately 2 wt% of O_2 was detected in the analysis of Si-kerf residue with an average calculated thickness of 0.01 μm [4]. The fact that a remaining powder was observed after melting (Fig. 4) could be explained by the presence of SiO_2 that might prevent complete melting of the Si-kerf residue at 1580 °C. The region being rich in Si for the sample II (Fig. 7) might be attributed to SiO_2 in the surface of the alloy due to the density difference. If the SiO_2 particles remain unchanged during melting, then they could potentially act as inoculant agents for the steel. Nevertheless, such behavior was not clearly observed in the current study. If the oxide layer on the particles surface breaks during the melting process, the Si can be dissolved in liquid iron and alloy the steel. As such, parameters like the density and stability of the added particles in the melt should be explored further. The addition of the particles prior the liquid state might promote the wetting of the particles with the steel and as such achieve a better dissolution. As a result, the Si being evenly dispersed in the analyzed samples could be explained accordingly.

Conclusions and Suggestions for Further Work

The current work is a preliminary study into the valorisation of Si-kerf residue in steel applications. The dissolution behavior of the Si-kerf residue into low alloyed steel was investigated, and the preliminary experiments indicate that

- Si particles dissolve rapidly in the steel alloy, and the addition of more Si-kerf typically results in a higher Si content in the final alloy.
- The microstructure of the samples is changing with the addition of the Si-kerf residue particles.
- Si is detected in all the analysed phases of the samples, while SiO_2 individual particles were not seen.
- Regions with higher Si content were observed on the outside surface of the alloy, confirming that part of the added Si-kerf remained undissolved.

Based on the results obtained from the present work, it is suggested that the addition of Si-kerf residue in different amounts should be studied in a wider range for the purpose of micro-alloying or deoxidation. Furthermore, the undissolved Si-kerf residue particles should be analyzed to examine the chemical composition and appeared phases. The effect of holding time and temperature on the behavior of Si particles in the steel at liquid state should also be addressed, since these parameters will affect the dissolution behavior. Finally, the introduction of Si-kerf residue particles after the melting of steel should be investigated further, in terms of its dissolution

behavior. Further research will also include a more in-depth metallographic analysis with the use of proper etching agents to examine whether remaining SiO_2 particles were left in the grains and in this way address whether Si-kerf could be used as inoculant agent. In addition, further experiments will try to address whether carbonized kerf residue or other type of additions can be used as inoculant agents.

References

1. Guo J, Liu X, Yu J, Xu C, Wu Y, Pan D et al (2021) An overview of the comprehensive utilization of silicon-based solid waste related to PV industry. Resour Conserv Recycl (Elsevier) 169:105450. https://doi.org/10.1016/J.RESCONREC.2021.105450
2. Yang S, Ma W, Wei K, Xie K, Wang Z (2019) Thermodynamic analysis and experimental verification for silicon recovery from the diamond wire saw silicon powder by vacuum carbothermal reduction. Sep Purif Technol (Elsevier) 228:115754. https://doi.org/10.1016/J.SEPPUR.2019.115754
3. Tomono K, Miyamoto S, Ogawa T, Furuya H, Okamura Y, Yoshimoto M et al (2013) Recycling of kerf loss silicon derived from diamond-wire saw cutting process by chemical approach. Sep Purif Technol (Elsevier) 120:304–309. https://doi.org/10.1016/J.SEPPUR.2013.10.014
4. Lim K (2018) Recovery and utilisation of Kerf Waste from silicon wafering process. Master's thesis, NTNU, Norwegian University of Science and Technology
5. Yang HL, Liu IT, Liu CE, Hsu HP, Lan CW (2019) Recycling and reuse of kerf-loss silicon from diamond wire sawing for photovoltaic industry. Waste Manag (Pergamon) 84:204–210. https://doi.org/10.1016/J.WASMAN.2018.11.045
6. Lu X, Miki T, Takeda O, Zhu H, Nagasaka T (2019) Thermodynamic criteria of the end-of-life silicon wafers refining for closing the recycling loop of photovoltaic panels. (Taylor & Francis) 20:813–825. https://doi.org/10.1080/14686996.2019.1641429. http://Www TandfonlineCom/Action/JournalInformation?Show=aimsScope&journalCode=tsta20#VmBm uzZFCUk
7. Wei D, Gao S, Kong J, Jin X, Jiang S, Zhou S et al (2020) Recycling silicon from silicon cutting waste by Al–Si alloying. J Clean Prod (Elsevier) 251:119647. https://doi.org/10.1016/J.JCLEPRO.2019.119647
8. Lin YC, Wang TY, Lan CW, Tai CY (2010) Recovery of silicon powder from kerf loss slurry by centrifugation. Powder Technol (Elsevier) 200:216–223. https://doi.org/10.1016/J.POWTEC.2010.02.028
9. Hachichi K, Lami A, Zemmouri H, Cuellar P, Soni R, Ait-Amar H et al (2017) Silicon recovery from Kerf Slurry waste: a review of current status and perspective. Silicon 10:4. (Springer) 10:1579–1589. https://doi.org/10.1007/S12633-017-9642-X
10. Jin X, Kong J, Zhou X, Xing P, Zhuang Y (2020) Recycling of silicon kerf loss derived from diamond-wire saw cutting process to prepare silicon nitride. J Clean Prod (Elsevier) 247:119163. https://doi.org/10.1016/J.JCLEPRO.2019.119163
11. Rodrigues TA, Duarte VR, Tomás D, Avila JA, Escobar JD, Rossinyol E et al (2020) In-situ strengthening of a high strength low alloy steel during wire and arc additive manufacturing (WAAM). Addit Manuf (Elsevier) 34:101200. https://doi.org/10.1016/J.ADDMA.2020.101200

12. Wu B, Pan Z, Ding D, Cuiuri D, Li H, Xu J et al (2018) A review of the wire arc additive manufacturing of metals: properties, defects and quality improvement. J Manuf Process (Elsevier) 35:127–139. https://doi.org/10.1016/J.JMAPRO.2018.08.001
13. Xia C, Pan Z, Polden J, Li H, Xu Y, Chen S et al (2020) A review on wire arc additive manufacturing: monitoring, control and a framework of automated system. J Manuf Syst (Elsevier) 57:31–45. https://doi.org/10.1016/J.JMSY.2020.08.008
14. Gennesson M, Daloz D, Zollinger J, Rouat B, Demurger J, Poirier D et al (2018) Inoculation in lab scale low alloyed steel castings. Minerals, metals and materials series. Springer International Publishing, Part F12, pp 577–585. https://doi.org/10.1007/978-3-319-72526-0_54
15. Arvola DA (2018) Grain refinement of high alloy stainless steels in sand and directionally solidified castings. Missouri University of Science and Technology
16. Ollilainen V, Kasprzak W, Holappa L (2003) The effect of silicon, vanadium and nitrogen on the microstructure and hardness of air cooled medium carbon low alloy steels. J Mater Process Technol (Elsevier) 134:405–412. https://doi.org/10.1016/S0924-0136(02)01131-7
17. Escrivà-Cerdán C, Ooi SW, Joshi GR, Morana R, Bhadeshia HKDH, Akid R (2019) Effect of tempering heat treatment on the CO_2 corrosion resistance of quench-hardened Cr-Mo low-alloy steels for oil and gas applications. Corros Sci (Pergamon) 154:36–48. https://doi.org/10.1016/J.CORSCI.2019.03.036
18. Fallahmohammadi E, Bolzoni F, Fumagalli G, Re G, Benassi G, Lazzari L (2014) Hydrogen diffusion into three metallurgical microstructures of a C-Mn X65 and low alloy F22 sour service steel pipelines. Int J Hydrogen Energy (Pergamon) 39:13300–13313. https://doi.org/10.1016/J.IJHYDENE.2014.06.122